Autonomous actuation of zero modes in mechanical networks far from equilibrium: Supplementary Material

Francis G. Woodhouse,[1, *] Henrik Ronellenfitsch,[2] and Jörn Dunkel[2]

[1]*Department of Applied Mathematics and Theoretical Physics, Centre for Mathematical Sciences,*
University of Cambridge, Wilberforce Road, Cambridge CB3 0WA, U.K.
[2]*Department of Mathematics, Massachusetts Institute of Technology,*
77 Massachusetts Avenue, Cambridge MA 02139-4307, U.S.A.

SINGLE MASS

Low temperature expansion

Here, we evaluate the low temperature expansion of the energy

$$H(x,y) = \tfrac{1}{2}\left[(|(1-x,y)|-1)^2 + (|(1+x,y)|-1)^2\right]$$

corresponding to the simple bead-spring model in Fig. 1 of the main text.

To lowest order in x and y, the non-interacting terms in the expansion $H(x,y) = x^2 + \frac{1}{4}y^4 + \cdots$ imply scalings $x \sim T^{1/2}$, $y \sim T^{1/4}$. Let $x = T^{1/2}u$ and $y = T^{1/4}v$. Then, expanding H in powers of $T^{1/2}$, write

$$T^{-1}H(x,y) = h_0(u,v) + T^{1/2}h_1(u,v) + O(T),$$

where

$$h_0(u,v) = u^2 + \tfrac{1}{4}v^4, \qquad h_1(u,v) = -u^2v^2 - \tfrac{1}{8}v^6.$$

We seek an expansion in T for the moment

$$\langle x^m y^n \rangle = \frac{\int_{-\infty}^{\infty}\int_{-\infty}^{\infty} x^m y^n e^{-H/T}\,dx\,dy}{\int_{-\infty}^{\infty}\int_{-\infty}^{\infty} e^{-H/T}\,dx\,dy}.$$

First, consider the partition function Z in the denominator. Changing to u and v, this reads

$$Z = T^{3/4}\iint e^{-h_0(u,v)}e^{-T^{1/2}h_1(u,v)+O(T)}\,du\,dv. \quad \text{(S1)}$$

Define the integral

$$I[f(u,v)] = \iint f(u,v)e^{-h_0(u,v)}\,du\,dv.$$

Since $T \ll 1$, the leading exponent in Eq. (S1) decays much faster than any others. Thus Z can be approximated by expanding $e^{-T^{1/2}h_1+O(T)} = 1 - T^{1/2}h_1 + O(T)$ to obtain

$$Z = T^{3/4}\left\{I[1] - T^{1/2}I[h_1] + O(T)\right\}.$$

An identical derivation gives

$$\iint x^m y^n e^{-H/T}\,dx\,dy$$
$$= T^{3/4+m/2+n/4}\left\{I[u^m v^n] - T^{1/2}I[u^m v^n h_1] + O(T)\right\}.$$

We can now assemble $\langle x^m y^n \rangle$. The above implies

$$T^{-m/2-n/4}\langle x^m y^n\rangle = \frac{I[u^m v^n] - T^{1/2}I[u^m v^n h_1] + O(T)}{I[1] - T^{1/2}I[h_1] + O(T)}.$$

Let $J[f] = I[f]/I[1]$. Expanding once more in T gives the general result

$$T^{-m/2-n/4}\langle x^m y^n\rangle$$
$$= J[u^m v^n] - T^{1/2}\left\{J[u^m v^n h_1] - J[u^m v^n]J[h_1]\right\} + O(T).$$

Thus the expansion amounts to the moment in the bare non-interacting Hamiltonian $H_0 = x^2 + \frac{1}{4}y^4$ corrected by its covariance with the strongest interactions.

Particular cases may be computed by evaluating the integrals. This can be done symbolically for general m, n; the particular cases of $\langle x^2 \rangle$ and $\langle y^2 \rangle$ read

$$\langle x^2 \rangle = \frac{1}{2}T + \rho T^{3/2} + O(T^2),$$

$$\langle y^2 \rangle = 2\rho T^{1/2} + \left\{\frac{9}{8} - \frac{7\rho^2}{2}\right\}T + O(T^{3/2}),$$

with $\rho = \Gamma(3/4)/\Gamma(1/4) \approx 0.34$.

Correlated noise: small τ

Upon introducing exponentially correlated noise generated by independent Ornstein–Uhlenbeck processes, the statistical distribution of the bead changes. We specialise to the overdamped limit, and rescale time to set $\gamma = 1$. Through an expansion in the correlation time τ, Ref. [1] shows that the mass follows an effective potential

$$H_{\text{eff}} = H + \tau\left[\tfrac{1}{2}|\boldsymbol{\nabla}H|^2 - T\nabla^2 H\right] + O(\tau^2). \quad \text{(S2)}$$

For the single bead, the full potential $H(x,y)$ can be substituted and moments of H_{eff} numerically evaluated, as shown in Fig. 1 of the main text with moments evaluated by quadrature in Mathematica.

To see the essential behaviour, we use expansion techniques at low temperature and small τ. When $T \ll 1$, the scaling $x \sim T^{1/2}$, $y \sim T^{1/4}$ still holds provided τ is small. Given this, the leading order terms read

$$H_{\text{eff}} = (\text{const}) + (1+2\tau)x^2 + \frac{1}{4}y^4 + \cdots$$

Thus the base effect of τ is to tighten the stiffness in x but leave y unchanged. This leading-order behaviour can also be captured by the unified coloured noise approximation [2, 3].

Provided the additional T factor in H_{eff} is carefully accounted for, the same low-temperature expansion as in the thermal case above can be applied. Omitting the irrelevant constant, H_{eff} has expansion terms

$$h_0(u,v) = (1 + 2\tau)u^2 + \tfrac{1}{4}v^4,$$
$$h_1(u,v) = -(1 + 4\tau)u^2v^2 - (\tfrac{1}{8} - \tfrac{1}{2}\tau)v^6 - \tau v^2.$$

Note the emergent v^2 term at non-zero τ in h_1, which will act to confine fluctuations in y as the temperature increases. Performing the integrations and expanding in τ eventually gives the leading order dependence of the variance ratio as

$$\frac{\langle y^2 \rangle}{\langle x^2 \rangle} = 4\rho(1 + 2\tau)T^{-1/2}$$
$$+ \tfrac{9}{4} - 15\rho^2 - \left(50\rho^2 - \tfrac{7}{2}\right)\tau + O(T^{1/2}).$$

Recasting this as a series first in τ, namely

$$\frac{\langle y^2 \rangle}{\langle x^2 \rangle} = 4\rho T^{-1/2} + \tfrac{9}{4} - 15\rho^2$$
$$+ \left(8\rho T^{-1/2} - 50\rho^2 + \tfrac{7}{2}\right)\tau + \cdots$$

reveals the temperature-dependent effect of correlation.

Correlated noise: large τ

In the limit of large τ, we can appeal to separation of equilibration time scales to derive an approximate distribution for the position $\boldsymbol{x} = (x, y)$.

In the overdamped limit, as before, $\boldsymbol{x}$ obeys

$$\dot{\boldsymbol{x}} = -\boldsymbol{\nabla}H(\boldsymbol{x}) + \boldsymbol{\xi}, \tag{S3}$$
$$\tau\dot{\boldsymbol{\xi}} = -\boldsymbol{\xi} + \boldsymbol{\eta}. \tag{S4}$$

First, Eq. (S4) implies that the stationary distribution of $\boldsymbol{\xi}$ is normal, with p.d.f. $p_{\boldsymbol{\xi}}(\boldsymbol{\xi}) \propto e^{-\tau|\boldsymbol{\xi}|^2/2T}$. Now, when τ is large, $\boldsymbol{x}$ equilibrates much faster than $\boldsymbol{\xi}$. Thus given the distribution of $\boldsymbol{\xi}$ we can approximate that of $\boldsymbol{x}$ by assuming $\dot{\boldsymbol{x}} \approx 0$ on time scales comparable with τ. Thus Eq. (S3) gives the relationship $\boldsymbol{\xi} \approx \boldsymbol{\nabla}H(\boldsymbol{x})$ between $\boldsymbol{\xi}$ and $\boldsymbol{x}$. Given $p_{\boldsymbol{\xi}}$, we can therefore approximate the p.d.f. $p_{\boldsymbol{x}}(\boldsymbol{x})$ of $\boldsymbol{x}$ through the inversion formula

$$p_{\boldsymbol{x}}(\boldsymbol{x}) = ||\boldsymbol{\nabla}\boldsymbol{\nabla}H|| \, p_{\boldsymbol{\xi}}(\boldsymbol{\nabla}H(\boldsymbol{x}))$$
$$\propto ||\boldsymbol{\nabla}\boldsymbol{\nabla}H|| \, e^{-\tau|\boldsymbol{\nabla}H(\boldsymbol{x})|^2/2T}, \tag{S5}$$

where $||\boldsymbol{\nabla}\boldsymbol{\nabla}H||$ denotes the absolute value of the determinant of the Hessian $\boldsymbol{\nabla}\boldsymbol{\nabla}H$ (that is, the Jacobian of the transformation by $\boldsymbol{\nabla}H$).

For $\tau/T \gg 1$ we can, like before, take an expansion to approximate moments of this distribution. Provided one accounts for the prefactor of the exponential, moments of $p_{\boldsymbol{x}}$ are related to moments of the Boltzmann distribution with effective potential $G(\boldsymbol{x}) = \frac{1}{2}|\boldsymbol{\nabla}H(\boldsymbol{x})|^2$ and effective temperature $T' = T/\tau$, since $p_{\boldsymbol{x}} \propto ||\boldsymbol{\nabla}\boldsymbol{\nabla}H||e^{-G/T'}$. Now, G has leading non-interacting terms $G = 2x^2 + \frac{1}{2}y^6 + \cdots$ implying scalings $x \sim T'^{1/2}$ and $y \sim T'^{1/6}$ (cf. the small-τ scalings $x \sim T^{1/2}$ and $y \sim T^{1/4}$). Following the same process as the low temperature expansion, by substituting for $x = T'^{1/2}u$ and $y = T'^{1/6}v$ and expanding in powers of $T'^{1/3}$ moments can be approximated as an expansion in T'. For conciseness we just compute the leading order here. We have

$$||\boldsymbol{\nabla}\boldsymbol{\nabla}H||e^{-G/T'} = \left[6v^2T'^{1/3} + O(\beta^{-2/3})\right]e^{-2u^2 - v^6/2},$$

implying

$$\iint x^m y^n p_{\boldsymbol{x}}(\boldsymbol{x}) \, dx \, dy$$
$$\approx 6T'^{2/3 + m/2 + n/6} \iint u^m v^{2+n} e^{-2u^2 - v^6/2} \, du \, dv.$$

Thus the normalisation Z for the p.d.f. $||\boldsymbol{\nabla}\boldsymbol{\nabla}H||e^{-G/T'}$ is

$$Z \approx 6T'^{2/3} \iint v^2 e^{-2u^2 - v^6/2} \, du \, dv = 2\pi T'^{2/3}$$

and the variances are

$$\langle x^2 \rangle \approx \frac{6T'^{5/3}}{Z} \iint u^2 v^2 e^{-2u^2 - v^6/2} \, du \, dv = \frac{T'}{4},$$
$$\langle y^2 \rangle \approx \frac{6T'}{Z} \iint v^4 e^{-2u^2 - v^6/2} \, du \, dv = \frac{2^{1/3}\Gamma(5/6)}{\pi^{1/2}}T'^{1/3}.$$

To lowest order, the variance ratio $\langle y^2 \rangle / \langle x^2 \rangle$ for large τ/T is therefore

$$\frac{\langle y^2 \rangle}{\langle x^2 \rangle} \approx \frac{2^{7/3}\Gamma(5/6)}{\pi^{1/2}} \left(\frac{\tau}{T}\right)^{2/3}.$$

As well as giving the power law for large τ, this shows that the T-dependence of the variance ratio changes from $T^{-1/2}$ at small τ to $T^{-2/3}$ at large τ. This is driven by the change in form of G compared to H: the prefactor $||\boldsymbol{\nabla}\boldsymbol{\nabla}H||$ does not affect the dominant scaling of the moments, so they scale with T as they would in the potential G.

NETWORKS: NON-DIMENSIONALISATION

The full dimensional equations of motion read

$$m\ddot{\boldsymbol{x}}_\alpha = -\frac{\partial H}{\partial \boldsymbol{x}_\alpha} - \gamma\dot{\boldsymbol{x}}_\alpha + \boldsymbol{F}_\alpha(\dot{\boldsymbol{x}}_\alpha; t),$$

with energy

$$H(\{\boldsymbol{x}_\alpha\}) = \frac{1}{2} \sum_{(\alpha,\beta)} k_{\alpha\beta}(|\boldsymbol{x}_\alpha - \boldsymbol{x}_\beta| - \ell_{\alpha\beta})^2.$$

Let κ and λ be typical scales for the spring moduli $k_{\alpha\beta}$ and rest lengths $\ell_{\alpha\beta}$. Rescale space and time as $\boldsymbol{x}_\alpha = \lambda\tilde{\boldsymbol{x}}_\alpha$ and $t = \tilde{t}\sqrt{m/\kappa}$, and use primes to denote $d/d\tilde{t}$. Then

$$\tilde{\boldsymbol{x}}''_\alpha = -\frac{\partial \tilde{H}}{\partial \tilde{\boldsymbol{x}}_\alpha} - \tilde{\gamma}\tilde{\boldsymbol{x}}'_\alpha + \tilde{\boldsymbol{F}}_\alpha(\tilde{\boldsymbol{x}}'_\alpha; \tilde{t}),$$

with dimensionless energy

$$\tilde{H}(\{\tilde{\boldsymbol{x}}_\alpha\}) = \frac{1}{2} \sum_{(\alpha,\beta)} \tilde{k}_{\alpha\beta}(|\tilde{\boldsymbol{x}}_\alpha - \tilde{\boldsymbol{x}}_\beta| - \tilde{\ell}_{\alpha\beta})^2$$

and dimensionless parameters

$$\tilde{\gamma} = \gamma/\sqrt{m\kappa}, \quad \tilde{k}_{\alpha\beta} = k_{\alpha\beta}/\kappa, \quad \tilde{\ell}_{\alpha\beta} = \ell_{\alpha\beta}/\lambda.$$

Note that the particle mass m has been scaled to unity. The dimensionless forcing function $\tilde{\boldsymbol{F}}_\alpha$ relates to the dimensional forcing through $\tilde{\boldsymbol{F}}_\alpha = (\kappa\lambda)^{-1}\boldsymbol{F}_\alpha(\lambda\sqrt{\kappa/m}\tilde{\boldsymbol{x}}'_\alpha; t\sqrt{m/\kappa})$.

Rescaling of noise

For white noise, $\boldsymbol{F}_\alpha = \boldsymbol{\eta}_\alpha(t)$ with $\langle \eta_{\alpha i}(t)\eta_{\beta j}(t') \rangle = 2\gamma T\delta_{\alpha\beta}\delta_{ij}\delta(t-t')$. Under our rescaling, this becomes another white noise $\tilde{\boldsymbol{F}}_\alpha = \tilde{\boldsymbol{\eta}}_\alpha(\tilde{t})$ correlated as $\langle \eta_{\alpha i}(t)\eta_{\beta j}(t') \rangle = 2\tilde{\gamma}\tilde{T}\delta_{\alpha\beta}\delta_{ij}\delta(t-t')$, with dimensionless temperature $\tilde{T} = T/(\kappa\lambda^2)$.

For exponentially correlated noise, $\boldsymbol{F}_\alpha = \boldsymbol{\xi}_\alpha(t)$ with $\langle \xi_{\alpha i}(t)\xi_{\beta j}(t') \rangle = \gamma T\delta_{\alpha\beta}\delta_{ij}e^{-|t-t'|/\tau}/\tau$. Under our rescaling, this becomes a process $\tilde{\boldsymbol{F}}_\alpha = \tilde{\boldsymbol{\xi}}_\alpha(\tilde{t})$ correlated as $\langle \tilde{\xi}_{\alpha i}(\tilde{t})\tilde{\xi}_{\beta j}(\tilde{t}') \rangle = \tilde{\gamma}\tilde{T}\delta_{\alpha\beta}\delta_{ij}e^{-|\tilde{t}-\tilde{t}'|/\tilde{\tau}}/\tilde{\tau}$ with dimensionless temperature $\tilde{T} = T/(\kappa\lambda^2)$ and correlation time $\tilde{\tau} = \tau\sqrt{\kappa/m}$. This becomes the white noise process above in the limit $\tilde{\tau} \to 0$.

Active forcing $\boldsymbol{F}_\alpha = \gamma_f\dot{\boldsymbol{x}}_\alpha(1 - |\dot{\boldsymbol{x}}_\alpha|^2/v^2)$ rescales to $\tilde{\boldsymbol{F}}_\alpha = \tilde{\gamma}_f\tilde{\boldsymbol{x}}'_\alpha(1 - |\tilde{\boldsymbol{x}}'_\alpha|^2/\tilde{v}^2)$ with dimensionless active friction coefficient $\tilde{\gamma}_f = \gamma_f/\sqrt{\kappa m}$ and target speed $\tilde{v} = \lambda\sqrt{\kappa/m}v$.

NETWORKS: HM–ZM COUPLING

Low temperature expansion

The symmetry of the single-mass example means that the HM and ZM decouple in the limit $T \to 0$. However, this is not necessarily the case in general: in a potential where x^2 and y^4 both scale with T, interaction terms xy^2 will also scale with T. Consider now a system of $n+1$ degrees of freedom $\{x_1, \ldots, x_n, y\}$, where the n variables x_i are HMs and y is a quartic IZM. In a low temperature expansion, the potential energy is

$$H = \sum_i a_i x_i^2 + \sum_i b_i x_i y^2 + A y^4 \quad \text{(S6)}$$

at lowest order, where $A > 0$ and all $a_i > 0$ but each b_i can be of either sign. We will evaluate the amplitudes $\langle y^2 \rangle$ and $\langle x_i^2 \rangle$.

To compute $\langle y^2 \rangle$, we can split the Boltzmann factor $e^{-H/T}$ into factors which can be integrated in each coordinate x_i sequentially, writing

$$e^{-H/T} = e^{-Ay^4/T} \prod_i e^{-(a_i x_i^2 + b_i x_i y^2)/T}.$$

Since

$$\int dx_i\, e^{-(a_i x_i^2 + b_i x_i y^2)/T} = C_i e^{(b_i^2/4a_i)y^4/T}$$

with $C_i = \sqrt{\pi T/a_i}$, splitting the Boltzmann factor allows us to reduce the computation to

$$\langle y^2 \rangle = \frac{\int dy\, y^2 e^{-Ay^4/T} \prod_i C_i e^{(b_i^2/4a_i)y^4/T}}{\int dy\, e^{Ay^4/T} \prod_i C_i e^{(b_i^2/4a_i)y^4/T}}.$$

The constant factors cancel and the exponentials combine, giving

$$\langle y^2 \rangle = \frac{\int dy\, y^2 e^{-\tilde{A}y^4/T}}{\int dy\, e^{-\tilde{A}y^4/T}} = \rho\sqrt{T/\tilde{A}},$$

where

$$\tilde{A} = A - \sum_i \frac{b_i^2}{4a_i}$$

and $\rho = \Gamma(3/4)/\Gamma(1/4)$ as before. That is, the variance $\langle y^2 \rangle$ is simply that of a single degree of freedom in an effective quartic potential $\tilde{A}y^4$. Note that $\tilde{A} < A$: the HM coupling increases the ZM amplitude.

The computation for $\langle x_m^2 \rangle$ is similar, albeit not quite as clean since the integral in x_m must incorporate the x_m^2 factor. Using the integral

$$\int dx_m x_m^2 e^{-(a_m x_m^2 + b_m x_m y^2)/T}$$
$$= C_m e^{(b_m^2/4a_m)y^4/T}\left(\frac{b_m^2}{4a_m^2}y^4 + \frac{T}{2a_m}\right),$$

the same approach as for $\langle y^2 \rangle$ reduces the computation to

$$\langle x_m^2 \rangle = \frac{\int dy\, \left(\frac{b_m^2}{4a_m^2}y^4 + \frac{T}{2a_m}\right)e^{-\tilde{A}y^4/T}}{\int dy\, e^{-\tilde{A}y^4/T}},$$

which is again simply a combination of moments in the effective potential $\tilde{A}y^4$. Thus

$$\langle x_m^2 \rangle = \frac{T}{2a_m}\left(1 + \frac{b_m^2}{8\tilde{A}a_m}\right). \tag{S7}$$

Observe that $\langle x_m^2 \rangle$ is only ever increased by introducing interactions b_m compared to its uncoupled amplitude $T/2a_m$. Thus not only do HM–ZM couplings increase ZM fluctuations, but they concomitantly increase HM fluctuations above those that would be guessed from naive equipartition. This effect is illustrated in Fig. S1 for 20 HMs of the network in Fig. 2 of the main text, for which interaction coefficients were determined by series expansion of the elastic energy in Mathematica.

There is one further effect to be noted. Not only does coupling increase the second moment $\langle x_m^2 \rangle$, but the mean $\langle x_m \rangle$ is displaced from zero by the asymmetry of the coupling. The same techniques again can be used to compute $\langle x_m \rangle$, this time using the integral

$$\int dx_m x_m e^{-(a_m x_m^2 + b_m x_m y^2)/T}$$

$$= -C_m e^{(b_m^2/4a_m)y^4/T}\frac{b_m}{2a_m}y^2,$$

giving

$$\langle x_m \rangle = \frac{b_m}{2a_m}\langle y^2 \rangle = \frac{b_m}{2a_m}\rho\sqrt{T/\tilde{A}}.$$

Conversely, the ZM is not displaced: symmetry means $\langle y \rangle = 0$.

The interaction-driven increase in $\langle x_m^2 \rangle$ could potentially be just a side effect of the non-zero mean $\langle x_m \rangle$. However, combining these results gives the mode variance as

$$\text{Var}(x_m) = \frac{T}{2a_m}\left(1 + \frac{(1-4\rho^2)b_m^2}{8\tilde{A}a_m}\right).$$

Since $1 - 4\rho^2 \approx 0.54 > 0$, the variance is indeed increased by HM–ZM coupling despite the shifted mean.

Correlated noise: small τ

When weak correlated noise is introduced into a general system with multiple HMs coupled to a ZM, its effect on the ZM can be neglected at low temperatures and short correlation times. The calculation goes as follows.

Take the same energy form as in Eq. (S6). Following Ref. [1] as in the single-mass example, when weak correlated noise of non-zero correlation time $\tau \ll 1$ is introduced the system follows an effective energy given by Eq. (S2). At low temperature, where $x^2 \sim T$ and $y^4 \sim T$, evaluating the gradients and keeping only the lowest order terms gives a first-order adjusted energy

$$H_{\text{eff}} = \sum_i a_i' x_i^2 + \sum_i b_i' x_i y^2 + A' y^4$$
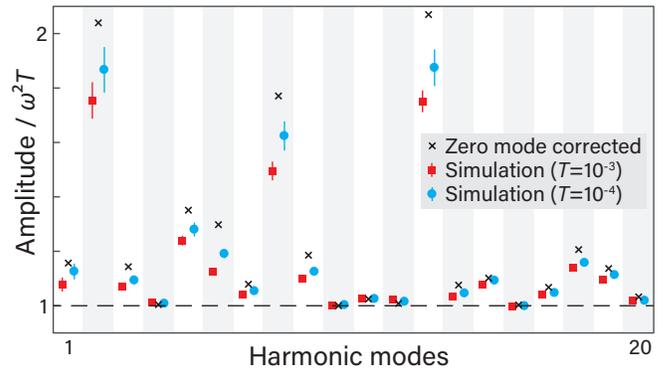
FIG. S1. Deviation from naive equipartition of the first 20 lowest-frequency HMs of the network in Fig. 2 of the main text. Markers show normalised amplitude $\langle c_i^2 \rangle/\omega_i^2 T$ numerically evaluated at $T = 10^{-3}$ (red squares) and $T = 10^{-4}$ (blue circles) compared to naive equipartition at 1 (dashed line) and with first-order correction in Eq. (S7) for interactions with the ZM (black cross). Error bars are estimated 95% confidence intervals. Interaction coefficients were determined by series expansion of the elastic energy in Mathematica.

where the τ-adjusted coefficients read

$$a_i' = a_i(1 + 2\tau a_i),$$
$$A' = A + \tfrac{1}{2}\tau\sum_i b_i^2,$$
$$b_i' = b_i(1 + 2\tau a_i).$$

It is clear that correlation $\tau > 0$ strengthens all couplings: $a_i' > a_i$, $A' > A$ and $|b_i'| > |b_i|$.

The approximate ZM amplitude $\langle y^2 \rangle$ is given by substituting these adjusted couplings into the formulae computed above. But, on computing the coupling-adjusted ZM amplitude

$$\tilde{A}' = A' - \sum_i \frac{b_i'^2}{4a_i'},$$

it transpires that $\tilde{A}' = \tilde{A}$. Since only this and T determine $\langle y^2 \rangle$, to first order in τ, the effect of correlations on the HMs is precisely compensated by its effect on the coupling terms to leave the ZM amplitude unchanged, that is, $\langle y^2 \rangle = \langle y^2 \rangle_{\tau=0}$ for $\tau \ll 1$.

Correlated noise: large τ

At large τ, the same timescale separation arguments as for the single bead can be used to derive asymptotic scalings for mode amplitudes in the overdamped limit. We sketch here the basic argument.

Once again take the same energy form as in Eq. (S6), this time appealing to a low $T' = T/\tau$ expansion. When τ is large, the mode degrees of freedom x_i and y equilibrate with the coloured noise much faster than the noise

changes. Equation (S5) then gives the effective p.d.f. for the modes. In this distribution, the scaling of the modes is driven by the exponential factor $e^{-G/T'}$ with potential $G(x_1, \ldots, x_n, y) = \frac{1}{2}|\boldsymbol{\nabla} H|^2$, where

$$ G = \sum_i \tfrac{1}{2}\left(2a_i x_i + b_i y^2\right)^2 + \tfrac{1}{2}y^2\left(\sum_i 2b_i x_i + 4Ay^2\right)^2 . $$

From a naive look at G one might infer that $x_i \sim T'^{1/2}$ and $y \sim T'^{1/4}$ (provided at least one $b_i \neq 0$) because of the non-interacting x_i^2 and y^4 terms at lowest order. However, there is an important subtlety: because the terms in the first sum, which are the lowest order terms, can be factorised as written, changing variables from x_i to $z_i = 2a_i x_i + b_i y^2$ eliminates y from the sum while only contributing a constant Jacobian factor to moment integrals. In other words, scalings are governed by the transformed potential

$$ \tilde{G} = \sum_i \tfrac{1}{2}z_i^2 + \tfrac{1}{2}y^2\left(\sum_i \frac{b_i}{a_i}(z_i - b_i y^2) + 4Ay^2\right)^2 . $$

Under $\tilde{G}$, the lowest non-interacting terms are z_i^2 and y^6. Thus $y \sim T'^{1/6}$—not $T'^{1/4}$—and $z_i \sim T'^{1/2}$, together implying $x_i \sim T'^{1/2}$. Therefore, the amplitudes $\langle x_i^2 \rangle$ and $\langle y^2 \rangle$ are asymptotically proportional to (T/τ) and $(T/\tau)^{1/3}$, respectively.

This argument shows that interaction terms do not affect the asymptotic scaling of the ZM and HMs with T/τ, with the ZM dominating HMs by a factor $\langle y^2 \rangle / \langle x_i^2 \rangle \sim \tau^{2/3}$ for large τ. Exact moments $\langle x_i^2 \rangle$ and $\langle y^2 \rangle$ can be formulated by the same process of telescoping x_i-integrals as above, but it is significantly more algebraically unwieldy due to the more complex exponent and the prefactor of

$$ ||\boldsymbol{\nabla}\boldsymbol{\nabla} H|| \propto \sum_i 2b_i x_i + \left(12A - \prod_j \frac{2b_j^2}{a_j}\right)y^2 $$

in Eq. (S5). We therefore do not compute the exact moment formulae here.

NETWORKS: FURTHER EXAMPLES

In Fig. 2 of the main text, a network with a single IZM is used to exemplify actuation by active correlated noise. In Fig. S2 we extend this to large correlation $\tau = 200$ and add two further examples displaying the same τ-dependent mode amplitude behaviour of HM suppression and ZM preservation. At long correlation times the amplitude asymptotics derived above for HMs ($\langle x_i^2 \rangle \sim \tau^{-1}$) and the ZM ($\langle y^2 \rangle \sim \tau^{-1/3}$) gradually take hold. Some modes are well into the long-τ regime by $\tau = 200$ while others are slower to approach it due to stronger higher-order terms.

Conversely, Fig. S3 shows that under-coordinated nodes can induce bistability in the structure, adversely affecting the mode statistics. In particular, a 2-coordinated node participating in the shown IZM has two equal-energy locations, meaning that bistable state transitions are easily triggered by the ZM actuation. This can adversely affect mode statistics if not eliminated at design time. In this case, though, the second stable location of the node overlaps with another, meaning that incorporating repulsive interactions between masses would lessen or eliminate the problem.
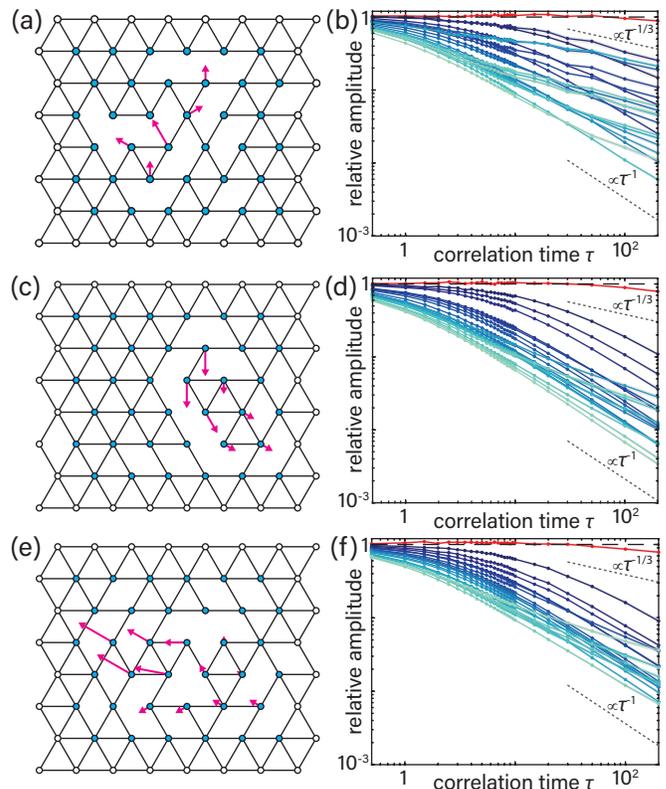
FIG. S2. Three examples of IZM actuation by correlated noise between $\tau = 0.5$ and $\tau = 200$. (a,c,e) Networks each with a single IZM (magenta) and pinned boundaries, with (a) as in Fig. 2 of the main text. (b,d,f) Thermal-relative mode amplitudes $\langle u_i^2 \rangle_\tau / \langle u_i^2 \rangle_{\tau=0}$ for the 21 lowest-eigenvalue modes of the networks in (a,c,e), on a log–log scale, with ZMs the uppermost red lines. Grey regions are approximate 95% confidence intervals; data computed from 20 independent realisations up to $t = 2 \times 10^4$ with $\delta t = 10^{-4}$ at values of τ between 0.5 and 200 indicated by points (see Computational Methods). Data in (a) is a superset of that of the main text Fig. 2(c), focussing here on large-τ behaviour. Shown gradient lines (dashed grey) are large-τ asymptotic predictions for the ZM ($\propto \tau^{1/3}$) and HMs ($\propto \tau$).

SELF-PROPULSIVE RAYLEIGH ACTIVITY

A mechanical network with Rayleigh activity has equations of motion

$$\ddot{\boldsymbol{x}}_\alpha = -\boldsymbol{\nabla}_\alpha H - \gamma\dot{\boldsymbol{x}}_\alpha + \gamma_f(1 - |\dot{\boldsymbol{x}}_\alpha|^2/v^2)\dot{\boldsymbol{x}}_\alpha. \qquad (S8)$$

The friction and active forcing can be condensed into a friction-like term as

$$\ddot{\boldsymbol{x}}_\alpha = -\boldsymbol{\nabla}_\alpha H - f(|\dot{\boldsymbol{x}}_\alpha|)\dot{\boldsymbol{x}}_\alpha,$$

where $f(u) = \gamma - \gamma_f + \gamma_f u^2/v^2$ is the effective friction coefficient. If $f(0) = \gamma - \gamma_f \equiv \gamma_0 < 0$, stationary states have negative effective friction and are unstable, with friction switching from negative to positive when $f(u) = 0$ at $|u| = v_0 \equiv \sqrt{|\gamma_0|/\gamma_f}v$. We can rewrite f in terms of γ_0 and v_0 as $f(u) = \gamma_0(1 - u^2/v_0^2)$.

Activation

As in the main text, considering a small perturbation of the rest state and decomposing into eigenmodes of the dynamical matrix gives linearised equations of motion in terms of the small mode amplitudes c_k with $|c_k| \ll 1$. For linearised Rayleigh friction, this gives

$$\ddot{c}_k = -\omega_k^2 c_k - \gamma_0\dot{c}_k.$$

Elementary analysis then shows that, provided $\gamma_0 < 0$, solutions $e^{\sigma t}$ have either a real 'overdamped' maximal growth rate $\max\sigma_k = \frac{1}{2}(|\gamma_0| + \sqrt{\gamma_0^2 - 4\omega_k^2})$ if $|\gamma_0| \geq 2\omega_k$, or a complex 'underdamped' growth rate with real part $\operatorname{Re}\sigma_k = |\gamma_0|/2$ if $|\gamma_0| < 2\omega_k$. Thus in either case, $\operatorname{Re}\sigma_k \geq |\gamma_0|/2$. The largest possible growth rate $\sigma_k = |\gamma_0|$ is achieved for a ZM, where $\omega_k = 0$.
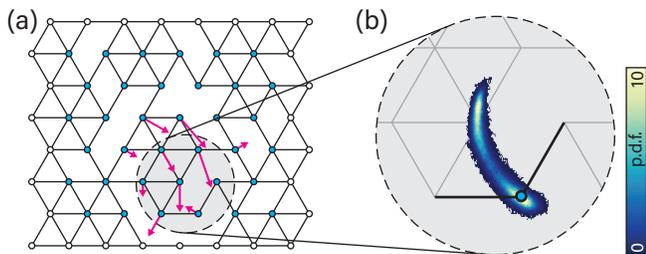
FIG. S3. Bistability in an IZM–participating node adds complexity to activation spectra. (a) A network with a single IZM, as before, containing a two-coordinated node whose position includes another equal-energy minimum by geometric symmetry. (b) Position histogram for the bistable node with $\tau = 6$. The node fluctuates into its other minimum, near which the overall mode spectrum is different. Note that in this case the bistability could be lessened by including hardcore repulsions between nodes.
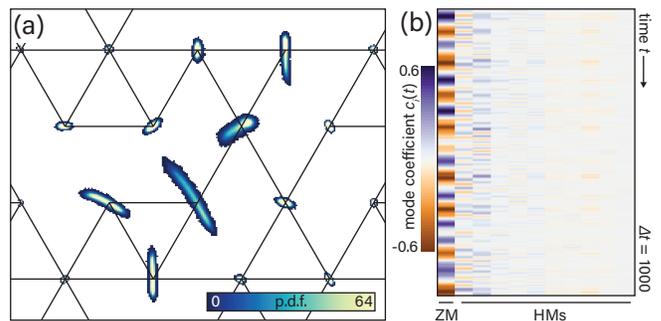
FIG. S4. Self-propulsive activity actuates IZMs in an oscillatory fashion (SM Video 4). (a) Per-node position histogram for the same network region as in Fig. 2b of the main text, but now actuated through Rayleigh forcing as in Eq. (S8). The ZM is prominent, while other nodes barely fluctuate. Parameters are $v_0 = 0.02$, $\gamma_0 = 1$, and $k_{\alpha\beta} = 1$, integrated at $\delta t = 10^{-5}$. (b) Example time trace over $\Delta t = 1000$ for the instance shown in (a) of mode coefficients $c_i(t)$ for the ZM and the ten lowest-frequency HMs. The ZM shows far stronger maxima than the HMs, with notable oscillatory behaviour.

Single mass: small γ_0

Unless mode k is a mechanism, growth of the mode will eventually be arrested by the combination of elastic forces and nonlinear effective friction terms, giving finite-amplitude oscillations. For the bead–spring example in the main text, we briefly examine this arrest process for small γ_0.

Formally, approximate solution for small $\epsilon \equiv |\gamma_0|$ is achieved by series expansion $\boldsymbol{x}(t) = \boldsymbol{x}_0(t) + \epsilon\boldsymbol{x}_1(t) + \cdots$. At $O(1)$, the equations of motion imply

$$\ddot{\boldsymbol{x}}_0 = -\boldsymbol{\nabla}H(\boldsymbol{x}_0).$$

Thus $\boldsymbol{x}_0$ simply corresponds to motion in the potential H, meaning $E_0 \equiv \frac{1}{2}|\dot{\boldsymbol{x}}_0|^2 + H(\boldsymbol{x}_0)$ is conserved.

Now, the range of maximum spatial extent occurs where $\dot{\boldsymbol{x}}_0 \sim 0$. Furthermore, higher-order dynamics set the velocity scale as $|\dot{\boldsymbol{x}}_0| \sim v_0$. Therefore, assuming $H(0) = 0$ is the energy minimum, conservation of E_0 between the origin and maximum extent implies $v_0^2 \sim H(\boldsymbol{x}_0)$ at the boundary. If v_0 is small, H can be approximated by its leading order expansion $H(x, y) \approx x^2 + \frac{1}{4}y^4$, meaning $y \sim v_0^{1/2}$ and $x \sim v_0$. Thus the variance ratio $\langle y^2\rangle/\langle x^2\rangle \sim 1/v_0$, and so the zero mode dominates as $v_0 \to 0$, fulfilling the same role as $T \to 0$ in the noise-driven case. (Indeed even with the same effective $1/\sqrt{T}$ scaling, since v_0^2 is a kinetic energy scale and so corresponds to T.)

Network IZM actuation

The same simultaneous ZM actuation and HM suppression in networks driven by active correlated noise
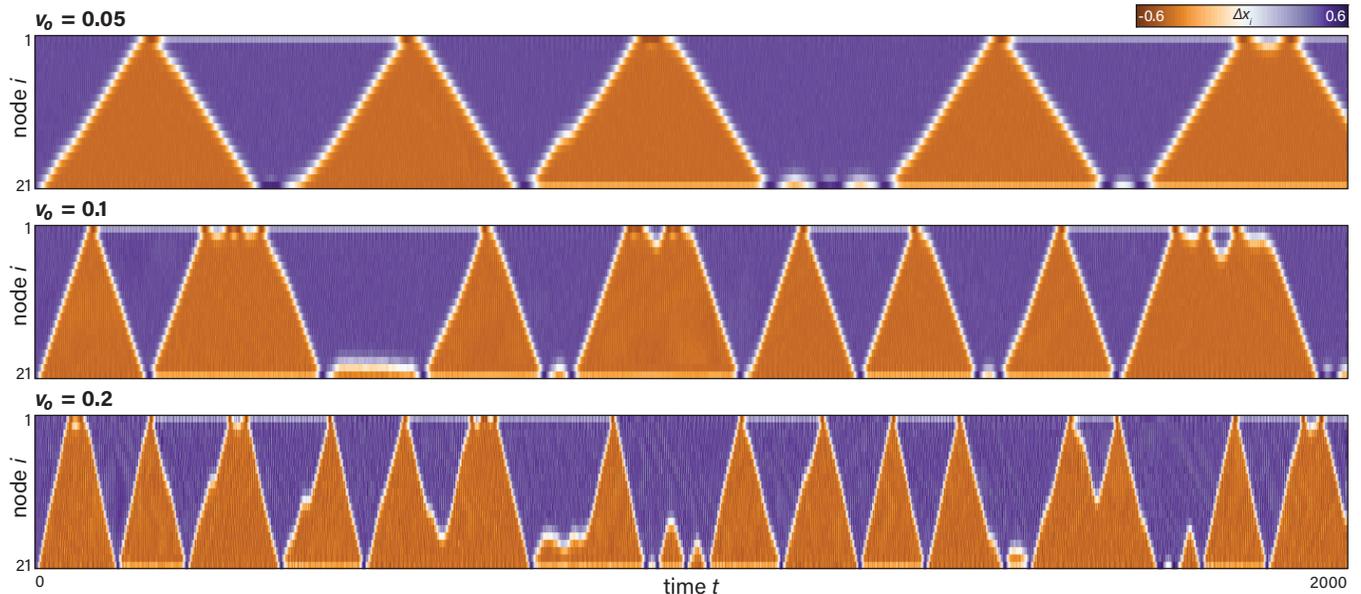
FIG. S5. Active mechanical SSH model as in Fig. 4 of the main text, with a different random perturbation to the initial conditions and $4\times$ longer time window.

persists with Rayleigh self-propulsive activity, as illustrated in Fig. S4a (see also SM Video 4). The mode coefficients $c_i(t)$ have oscillatory temporal structure (Fig. S4b), giving potentially useful actuation behaviour that can be controlled by varying parameters of the activity.

Active mechanical SSH soliton

In Fig. 4 of the main text, we show realisations of the mechanical SSH model with self-propulsive activity at three different effective propulsion speeds v_0, exemplifying how activity excites the underlying mechanism leading to a self-propelled soliton-like domain boundary. While the domain propagates cleanly most of the time, there are occasional defects visible where the domain slows, stalls or reverses because of the complex interactions between the activity-driven oscillatory fluctuations of the nodes (main text Fig. 4b, $v_0 = 0.1$ and $v_0 = 0.2$). These imperfection phenomena can be seen in more detail in Fig. S5, where we exhibit a longer-time run of the same model and parameters as in the main text with a different random perturbation to the initial conditions. Stalls and reversals mid-chain are rare, with the endpoints being, perhaps unsurprisingly, more prone to imperfection because of the particular complexity of the mechanism there. We emphasise that this model does not have any random noise added, beyond an initial perturbation; these reversals are the result of complex interactions between the fluctuating self-propelled nodes.

COMPUTATIONAL METHODS

Single bead statistics

High-quality independent position samples for the single mass in Fig. 1 of the main text were computed by integrating the coupled overdamped equations

$$\dot{\boldsymbol{x}} = -\boldsymbol{\nabla} H(\boldsymbol{x}) + \boldsymbol{\xi}, \quad \tau\dot{\boldsymbol{\xi}} = -\boldsymbol{\xi} + \boldsymbol{\eta},$$

with $\langle \eta_i(t)\eta_j(t')\rangle = 2T\delta_{ij}\delta(t-t')$, up to a stopping time $t = t_{\text{stop}}$ and taking the endpoint $\boldsymbol{x}(t = t_{\text{stop}})$ as a sample. Taking a large set of N samples was accelerated by massively parallel GPU computing to perform each integration in one GPU thread (NVIDIA Titan X Pascal).

Network design

We design networks containing isolated IZMs by direct numerical minimisation of the lowest eigenvalue ω_1^2 of the dynamical matrix D_{ij} with respect to the stiffnesses $k_{\alpha\beta}$. Starting from uniformly random initial stiffnesses on a triangular lattice and constraining them to $0 \leq k_{\alpha\beta} \leq 1$, the gradient-based L-BFGS-B algorithm as implemented in SciPy 1.0 [4] generally converges to a network in which some of the stiffnesses and ω_1^2 are exactly zero, and which therefore exhibits an IZM. Since IZMs are topological, independent of the precise values of the nonzero $k_{\alpha\beta}$ [5], a network containing the same IZM is then obtained by removing the zero-stiffness bonds and setting the remaining stiffnesses to 1.

Network simulations

All numerical integration for networks was performed by Euler/Euler–Maruyama integration of the appropriate system of equations. Mode statistics were determined from M independent trajectories. Each trajectory was started from equilibrium, integrated over a time 100 and discarded to randomise initial conditions, and then sampled up to a time $t = t_{\max}$. The parameters M and $t_{\max}$ are given in figure captions.

Each trajectory was subsampled at a resolution $\Delta t = 1$ to compute statistics on $n = t_{\max}$ samples. The variance $\bar{\sigma}_i^2$ of the mean $\bar{x}$ of a statistic x computed from trajectory i was estimated through [6, 7],

$$\bar{\sigma}_i^2 = \frac{\sigma_i^2}{\sqrt{n}} \left[1 - \frac{2}{n} \sum_{k=1}^{\lfloor \sqrt{n} \rfloor} (n - k)\rho_i(k) \right],$$

where $\rho_i(k)$ is the normalised naively-estimated autocorrelation at lag k and the upper truncation at $\lfloor \sqrt{n} \rfloor$ omits heavily biased autocorrelation estimates that are in practice expected to be near zero [6]. Per-trajectory errors are then combined as independent variances to yield the overall estimated standard error $\bar{\sigma}$ of $\bar{x}$. Approximate 95% intervals are shown in figures as $\bar{x} \pm 1.96\bar{\sigma}$.

EXPERIMENTAL METHODS

The stiff-jointed network in Fig. 3a of the main text was constructed using flat brackets of dimensions $3.66 \, \text{cm} \times 0.75 \, \text{cm}$ which were laser cut from transparent acrylic of thickness 1.2 mm. For the pin joints connecting the brackets, 2–56 thread size, 1/2 in long nylon screws and nuts were used. Where only three or four brackets were jointed together, the joints were strengthened using nylon washers. The pins corresponding to the outermost nodes were fastened directly to a 9 in diameter circular plate, laser cut from acrylic of circa 1 cm thickness. The plate was then mounted on top of an Eminence Speakers Delta-12LFA, 12 in, 500 W speaker (Eminence Speaker LLC, Eminence KY), which was mounted on an optical table and driven using a Pyle PQA4100 amplifier (Pyle Audio, Brooklyn NY). Video was acquired at 1920×1080 pixels resolution and a frame rate of 30 Hz using an Olympus consumer digital camera (Olympus America Inc., Center Valley PA) at 40 mm focal length mounted on a tripod. The positions of the nodes were tracked using the `trackpy 0.4.1` package [8].

To actuate the network, the speaker was driven by a signal comprising a carrier frequency and Ornstein–Uhlenbeck noise with subsecond correlation. In these experiments, it is the carrier frequency actuation that is mimicking the active driving, not the added correlated noise, as interactions between the network and the
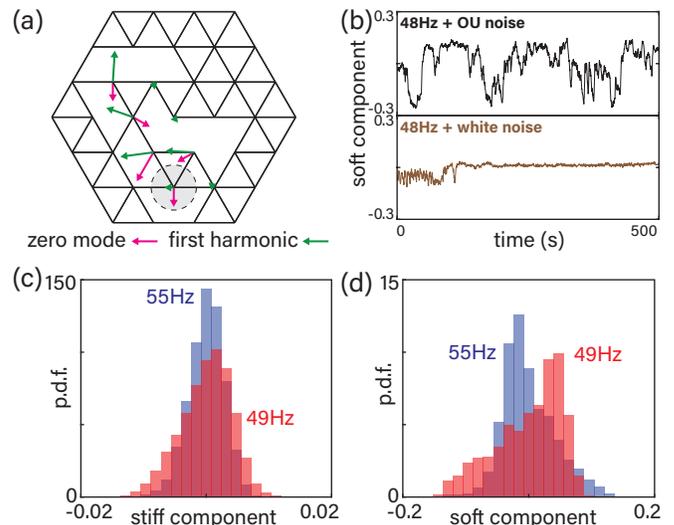
FIG. S6. Experimental actuation method affects relative ZM–HM statistics. (a) Diagram of the experimental network shown in the main text Fig. 3, with both the ZM and the lowest-frequency HM shown. (b) Traces of the soft component c_2, defined in the text, of the node highlighted in (a) for correlated and uncorrelated additions to 48 Hz carrier frequency actuation. The upper adds 15% Ornstein–Uhlenbeck noise of correlation time $(1/350)$ s while the lower adds 15% white noise of identical intensity. Short-time correlation is necessary to keep the network exploring the energy landscape. (c,d) Histograms of soft (c) and stiff (d) components c_1 and c_2 for two frequenies of actuation, both with 20% added Ornstein–Uhlenbeck noise of correlation time $(1/345)$ s. Changing the carrier frequency controls the mode actuation, with 55 Hz giving greater ZM actuation relative to non-ZM modes compared to 49 Hz. Note the 10× larger scale in the soft component (d) compared to the stiff component (c).

shaken baseboard drive stochastic forcing. The correlated noise here functions instead as a crucial component to prevent sticking of the network in resonance-related metastable states, discussed below.

To explore the effect of different forms of drive, we focus on one particular node which participates in both the IZM and the lowest-frequency HM (highlighted in Fig. S6a) in near-perpendicular directions. Given its positions $\boldsymbol{x}_i = (x_i, y_i)$ at frames i, rescaled such that the distance between adjacent nodes is 1 in the reference configuration, we compute the covariance matrix $\text{Cov}(x_i, y_i)$. The orthonormal eigenvectors $\boldsymbol{v}_1, \boldsymbol{v}_2$ of the covariance matrix corresponding to the eigenvalues $\lambda_1 < \lambda_2$ then represent the stiff ($\boldsymbol{v}_1$) and soft ($\boldsymbol{v}_2$) perpendicular directions. We then use the stiff and soft components $c_1 = \boldsymbol{x} \cdot \boldsymbol{v}_1$ and $c_2 = \boldsymbol{x} \cdot \boldsymbol{v}_2$ as simple representations of HM-related and ZM-dominated actuation.

Figure S6b shows the importance of short but non-zero correlation in the noise added to the carrier frequency. We compare the soft component c_2 from experiments using 48 Hz actuation with 15% Ornstein–Uhlenbeck noise

of correlation $(1/350)$ s versus 15% white noise of identical intensity. This exemplifies how correlated noise keeps the network exploring configuration space, while even with white noise it quickly sticks in a metastable state.

Changing the carrier frequency, rather than the added noise, controls the effective activity of the nodes leading to different positional distributions. Figure S6c,d gives histograms of the components c_1 and c_2 for actuation with carrier frequencies of 49 Hz (used in the main text Fig. 3) and 55 Hz plus 20% $(1/345)$ s-correlated Ornstein–Uhlenbeck noise. The latter tightens in the stiff direction compared to the former, signifying greater ZM actuation relative to HMs, while the soft component changes shape more markedly as a result of the complex interactions of the network with the shaken baseboard.

––––––––––

* Present address: Mathematical Institute, University of Oxford, Andrew Wiles Building, Radcliffe Observatory Quarter, Woodstock Road, Oxford OX2 6GG, U.K.; Correspondence to: francis.woodhouse@maths.ox.ac.uk

[1] É. Fodor, C. Nardini, M. E. Cates, J. Tailleur, P. Visco, and F. van Wijland, Phys. Rev. Lett. **117**, 038103 (2016).

[2] P. Jung and P. Hänggi, Phys. Rev. A **35**, 4464 (1987).

[3] C. Maggi, U. M. B. Marconi, N. Gnan, and R. Di Leonardo, Sci. Rep. **5**, 10742 (2015).

[4] E. Jones, T. Oliphant, P. Peterson, *et al.*, "SciPy: Open source scientific tools for Python," (2001–), [http://www.scipy.org/].

[5] C. L. Kane and T. C. Lubensky, Nat. Phys. **10**, 39 (2014).

[6] C. J. Geyer, Stat. Sci. **7**, 473 (1992).

[7] T. J. Witt and N. E. Fletcher, Metrologia **47**, 616 (2010).

[8] D. B. Allan, T. Caswell, N. C. Keim, and C. M. van der Wel, "trackpy v0.4.1," (2018), [https://doi.org/10.5281/zenodo.1226458].